Prebiotic Chemistry and Atmospheric Warming of Early Earth By An Active Young Sun

V. S. Airapetian[1], A. Glocer[1], G. Gronoff[2], E. Hébrard[1] W. Danchi[1]

Affiliations:

[1]NASA Goddard Space Flight Center, 8800 Greenbelt Rd, Greenbelt, MD, USA

[2]Science Systems and Application, Inc. & NASA Langley Research Center, Hampton, VA, USA

Nitrogen is a critical ingredient of complex biological molecules [1]. Molecular nitrogen, however, which was outgassed into the Earth's early atmosphere [2], is relatively chemically inert and nitrogen fixation into more chemically reactive compounds requires high temperatures. Possible mechanisms of nitrogen fixation include lightning, atmospheric shock heating by meteorites, and solar ultraviolet radiation [3,4]. Here we show that nitrogen fixation in the early terrestrial atmosphere can be explained by frequent and powerful coronal mass ejection events from the young Sun - so-called superflares. Using magnetohydrodynamic (MHD) simulations constrained by Kepler space telescope observations, we find that successive superflare ejections produce shocks that accelerate energetic particles, which would have compressed the early Earth's magnetosphere. The resulting extended polar cap openings provide pathways for energetic particles to penetrate into the atmosphere and, according to our atmospheric chemistry simulations, initiate reactions converting molecular nitrogen, carbon dioxide and methane to the potent greenhouse gas nitrous oxide as well as hydrogen cyanide, an essential compound for life.

Furthermore, the destruction of N_2, CO_2 and CH_4 suggests that these greenhouse gases cannot explain the stability of liquid water on the early Earth. Instead, we propose that the efficient formation of nitrous oxide could explain a warm early Earth.

MAIN TEXT

Here we develop a new concept of the rise of prebiotic chemistry on early Earth that suggests abiotic nitrogen fixation mediated by the energy flux from paleo solar eruptive events. The flare statistics of *Kepler* data suggests that the frequency of occurrence of superflares with energies > 5 x 10^{34} erg observed on G-type dwarfs follows a power-law distribution with spectral index between (α=− 2.0), which is comparable to those observed on dMe stars and the Sun [5,6]. If the occurrence rate of superflares on young solar-like ~ 0.1 events/day [6], then, the frequency of super Carrington-type flare events with E ~ 10^{33} ergs on the early Sun ($\leq$ 0.5 Gyr) is expected to be ~ 250 events per day! Current data suggest that powerful solar flares (over X5 type) are usually associated with fast ($\geq$ 1000 km s^{-1}) wide (θ > 100°) coronal mass ejections (CMEs) and high-fluence solar energetic particle (SEP) events with kinetic energies up to 10^{33} ergs [7-9]. Tree ring data have recently provided evidence in favor of past superflares from the Sun [10,11]. Their energy is a factor of 2-3 greater than that suggested for the famous Carrington-type CME event [12]. Recent direct measurements of surface longitudinal magnetic fields on young solar-type stars imply that our young Sun had generated at least 10 times greater magnetic flux than that observed in the current Sun [13]. The stronger magnetic flux produces frequent and energetic flares, fast and wide coned CMEs and associated energetic SEP events with energies up to 10^{36} ergs. Our calculations suggest that the probability of CME striking the Earth is about 5% [14]. In the “perfect” magnetospheric storm, when the incoming cloud magnetic field, B_z component is sheared with respect to the Earth's magnetic field, the frequency of CME impacts

is > 1 event per day! To model a CME event and its effects on the Earth's magnetosphere, we used the Space Weather Modeling Framework (SWMF) available through the Community Coordinated Modeling Center (CCMC) (see Supplementary Material). We assumed a steady state paleo solar wind at 0.7 Gyr with the mass loss rate of 1.7×10^{-12} M_{sun}/yr and the wind speed of 700 km/s as obtained from the 3D MHD young Sun's wind model [15] and a Carrington-type CME cloud propagating at the radial speed of 1800 km/s with the total energy of 2×10^{33} erg [12]. Figure 1 presents a 2D map of the steady-state plasma density superimposed by magnetic field lines for the magnetospheric configuration in the Y=0 plane corresponding to the initial 30 minutes of the simulations, when the Earth's magnetosphere was driven only by dynamic pressure from the paleo-solar wind. The left panel of Figure 1 shows the steady state paleo solar wind compresses the Earth's magnetosphere to ~ 9 R_E. The right panel of Figure 1 shows the state of the magnetosphere two hours later when the CME cloud hits the Earth's magnetosphere (also see the movies in Supplementary Material). At this time, the solar wind dynamic pressure and the magnetic reconnection between the southward directed CME's cloud magnetic field and northward Earth's dipole field pushing the dayside magnetosphere earthward reducing the magnetopause stand-off distance from 9 to ~1.5 Earth's radii. The CME drives large field aligned current distributions and produces significant disturbance of the magnetospheric field shifting the boundary of the open-closed field shifts to 36° in latitude and producing a polar cap opening to 70% of the Earth's dipole magnetic field. In the current version, we used the dipole magnetic field of the current Earth, however paleomagnetic studies of the Earth's ancient rocks suggest that the field was weaker [16]. This suggests that the fraction of the open field used in our model represent only a lower bound. Energetic particles accelerated in shocks driven by successive flare/CME events (see for example [17]) can then efficiently penetrate the early terrestrial

atmosphere through the expended polar cap region.

We applied the Aeroplanet model [18] to simulate the atmospheric chemistry of the nitrogen-dominated (80% N_2, 20% CO_2 and 0.03% CH_4) primitive Earth's atmosphere [19]. The upper boundary of the atmosphere at 100 km is exposed to the steady state XUV flux with the spectrum reconstructed for the early Sun at 0.7 Gyr [20] and to energetic protons with the energy flux of 5 x 10^{11} protons/cm^2/MeV at 0.1 MeV with the spectral index of the energy spectrum of -2.15 representative of the Jan 20, 2005 SEP event and the energy range within 1 GeV [21]. The model calculates photoabsorption of the EUV-XUV flux from the early Sun (see Figure 2) and particle (electron and proton) fluxes to compute the corresponding fluxes at the atmospheric altitudes between 200 km and the surface. These fluxes are used to calculate the photo and particle impact ionization/dissociation rates of the atmospheric species producing secondary electrons due to ionization processes. Then, using the photon flux and the photoionization-excitation-dissociation cross-sections, the model calculates the production of ionized and excited state species and as a result, photoelectrons. In our steady-state model of the early Earth's atmosphere, energetic precipitating protons from an SEP event impacted the middle and low atmosphere and produce ionizations, dissociations, dissociative ionizations, and excitations of atmospheric species and as a result, secondary electrons. The model includes 117 neutral chemical reactions. The destruction of N_2 into reactive nitrogen, $N(^2D)$ and $N(^4S)$ and the subsequent destruction of CO_2 and CH_4 produces NO, CO, CH and NH in the polar regions of the atmosphere as shown in Figure 3 (see Supplementary Material).

Our model predicts the formation of abundant NO and NH molecules and efficient formation of N_2O through NO + NH → N_2O + H with the major sink through the reaction N_2O + H → OH + N_2 (see the pathway diagram in Figure 3). Photolysis of N_2O via the reaction

93 pathway $N_2O + h\nu \rightarrow N_2+O(^1D)$ is not an efficient loss channel for N_2O, because of absorption
94 of solar flux shorter than 2300 Å by CH_4. Atmospheric N_2O steady-state density reaches a
95 concentration with the mixing ratio of 2 and 20 ppbv at 30 km in the 1 PAL (present atmospheric
96 level) atmosphere with 100% (solid line) and 10% (dashed line) of the maximum photochemical
97 destruction rate, as shown in Figure 4a. The derived value at 100% of the photodestruction rate
98 should be considered as a lower bound, because our model does not account for a number of
99 factors including the eddy diffusion and convection effects, the effects of Rayleigh scattering of
100 solar EUV radiation in the atmosphere and formation of hazes that significantly reduces the
101 photo-destruction rate of nitrous oxide, and therefore increases the production of N_2O. Thus, the
102 model with 10% of the maximum photo-destruction rate probably better represents the density
103 profiles when all factors are accounted for. The steady-state density of N_2O reaches 20 to 3000
104 ppbv in the 2 PAL model with 100% (solid line) and 10% (dashed line) of the maximum
105 photochemical destruction rate, as shown in Figure 4b. The choice of 2 PAL in Figure 4b is
106 consistent with compelling evidence that the atmospheric pressure of early Earth was enhanced
107 by a factor of 2-3 [22]. Another factor affecting the equilibrium mixing ratios of Figure 4 is the
108 representative energy of SEP events, which could be greater than that assumed in the model.
109 Laboratory experiments report the production of nitrogen oxides and N_2O when N_2-CO_2 mixture
110 that simulates the early Earth atmosphere was exposed by lightning and coronae discharges [23].
111 Enhanced production of nitrous oxide in the lighting experiments are caused by energetic
112 electrons accelerated in the discharge and UV emission. Other evidence for the role of energetic
113 particles in N_2O production comes from direct observations of its enhancement by 3% associated
114 with thunderstorm events [24].

115 The efficient production of N_2O in our model offers a solution to warming the early

116 Earth. The 0.7 Gyr old Sun was 25-30% fainter than the present-day Sun [25], which would be
117 insufficient to support liquid water on the early Earth contrary to geological evidence of that time
118 [26]. Current models of atmospheric warming offer solutions of this problem, commonly known
119 as Faint Young Sun (FYS) paradox due to a large atmospheric concentration of CO_2, H_2O, CH_4
120 or N_2 and H_2 [27]. However, as our model implies, these molecules will be efficiently dissociated
121 due to photo-collisional processes driven by SEPs from the young Sun, which is consistent with
122 the recent mineralogical data [28]. Instead, the production of CH, NH and NO sets stage for the
123 formation of N_2O, HCN and other N-containing species in the lower parts of the atmosphere.
124 HCN concentration reaches up to tens ppmv in the lower atmosphere. The calculated production
125 rate of HCN in the low atmosphere is driven by the following major reactions: NO + CH →
126 HCN + O, CH_2 + N(^{4}S) → HCN + H, CH_3 + N(^{4}S) → HCN + H + H, CH + CN → HCN + H,
127 N_2O + CH → HCN + NO. Organic molecules may subsequently rain out into surface reservoirs
128 and engage in higher order chemistry producing more complex organics. For example, further
129 HCN polymerization is known to produce various amino acids, the building blocks of proteins
130 [29]. Production of other types of soluble N-containing species (NH_3, HNO, NO) by particles
131 may have provided a massive dose of nitrogen "fertilizer" to early surface biology on terrestrial
132 planets.

133 Thus, our concept implies that early Sun's activity provided a window of opportunity for
134 prebiotic life on Earth. The proposed model also redefines the conditions of habitability not just
135 in terms of a "liquid water zone", but as a biogenic zone (BZ), within which the stellar energy
136 fluxes are high enough to ignite reactive chemistry that produces complex molecules crucial for
137 life. As a by-product, this chemistry forms greenhouse gasses that may efficiently keep the
138 atmosphere warm for liquid water to exist. The model predictions can tested by observing broad

and deep molecular absorption lines of N_2O at 4.5 μm and 7.9 μm and HCN absorption features at 3 and 14.3 μm using James Webb Space Telescope NIRSpec and MIRI observations of primitive terrestrial-type atmospheres around active stars.

FIGURES

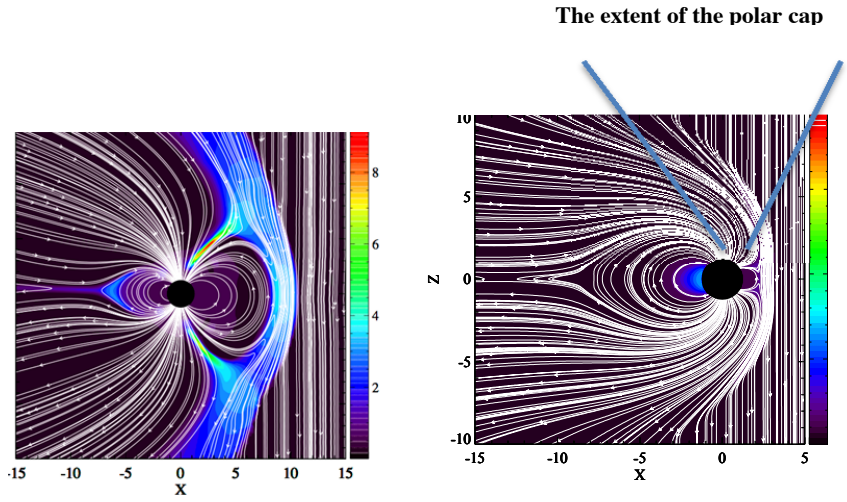

a. *b.*

Figure 1. The initial (panel a) and the final state (panel b) magnetic field lines in white) and the plasma pressure (in color) of the Earth's magnetosphere due to the CME event (Airapetian et al. 2015)

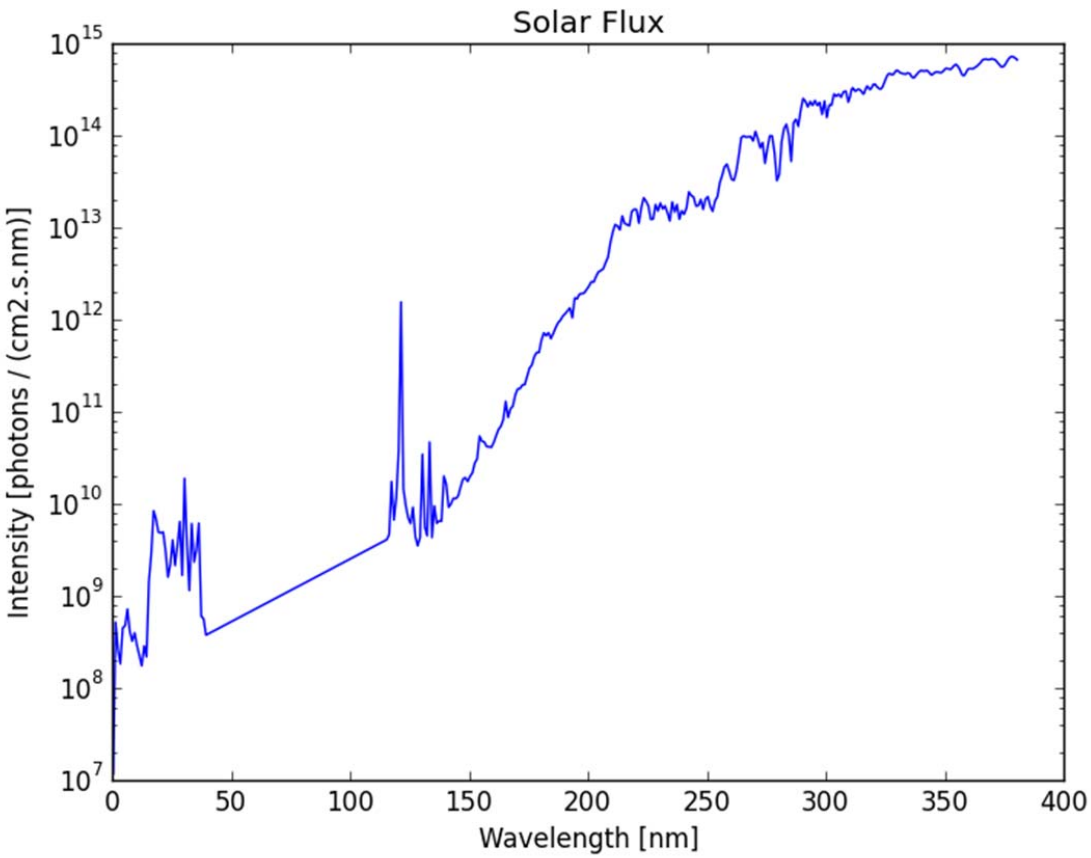

156

157 *Figure 2. Spectrum of the young Sun's XUV flux at 0.7 Gyr [20]*

158

159

160

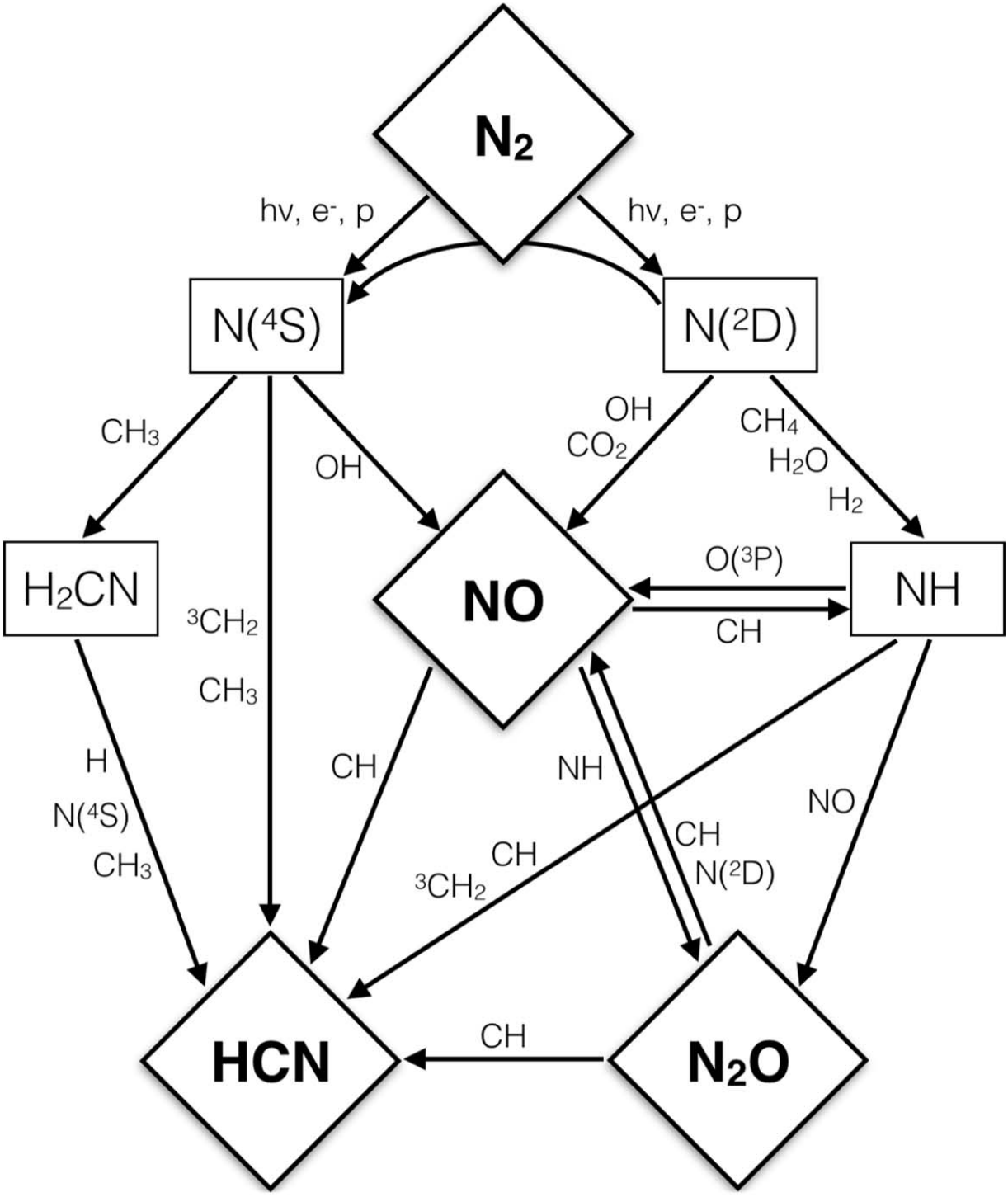
N2
hv, e-, p
hv, e-, p
N(4S)
N(2D)
CH3
OH
OH
CO2
CH4
H2O
H2
H2CN
NO
O(3P)
NH
CH
3CH2
CH3
H
N(4S)
CH3
CH
NH
NO
CH
3CH2
CH
N(2D)
HCN
CH
N2O

Figure 3. The pathway diagram of abiotic production of odd nitrogen and nitrogen-bearing compounds including nitrous oxide and hydrogen cyanide due to photo and collisional dissociation and ionizations caused by XUV solar flux and SEP particle flux.

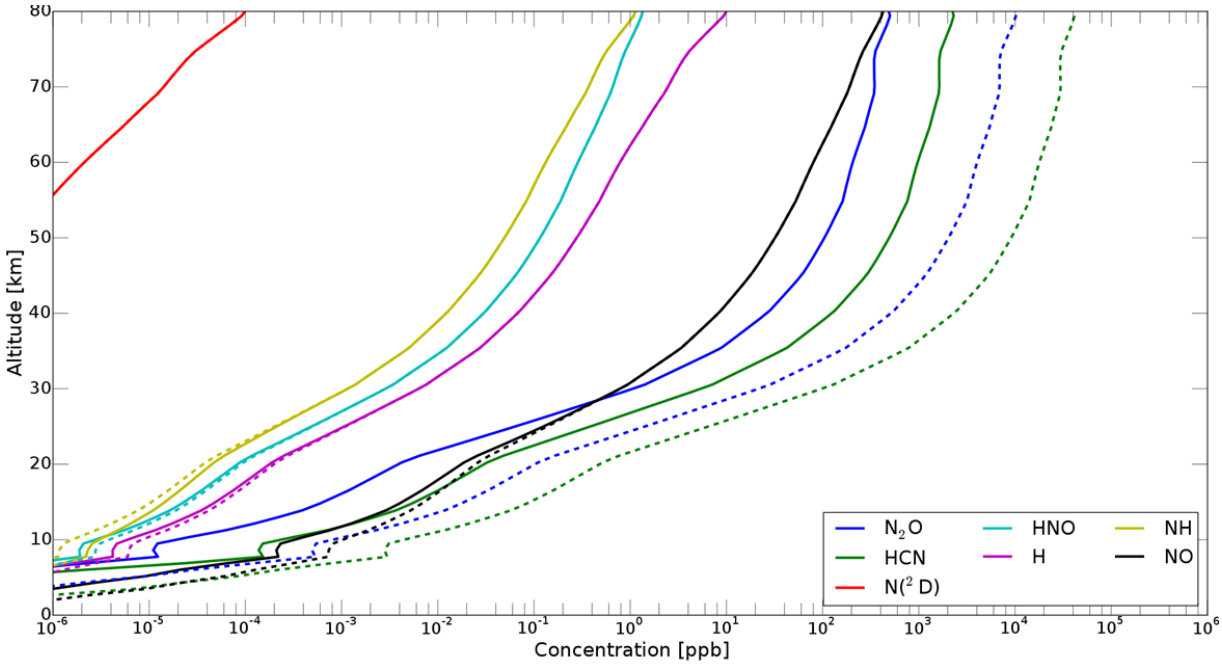

a.

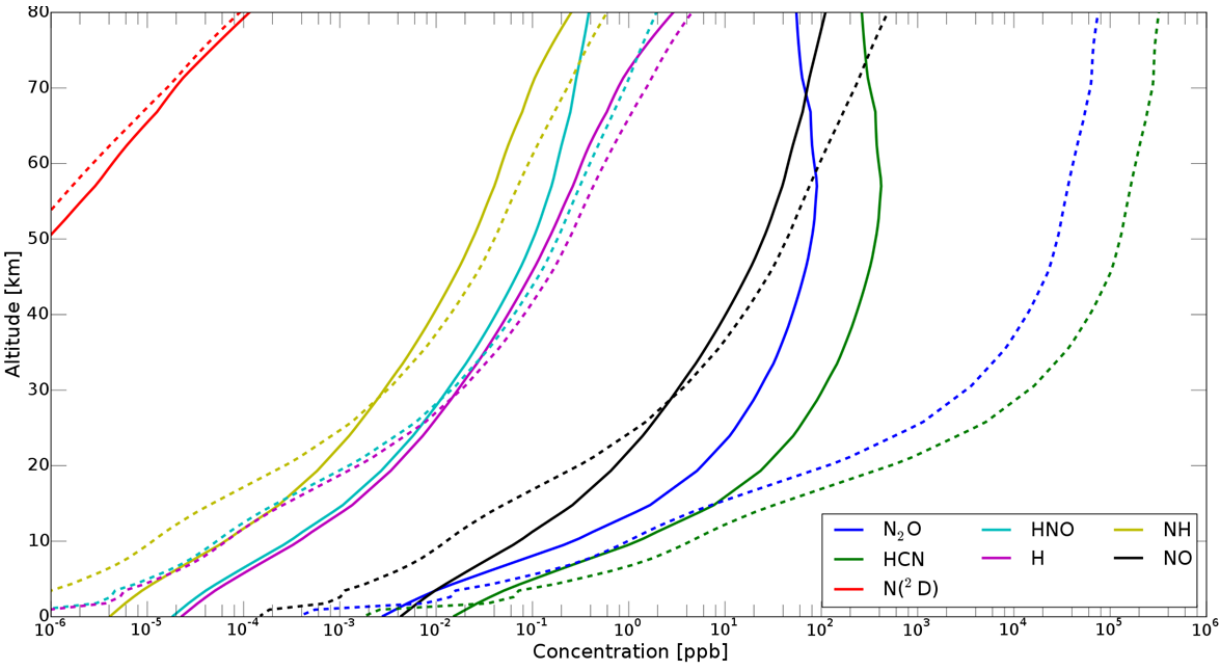

b.

Figure 4. Radial profiles of the steady-state mixing ratios of various species produced by incoming flux of primary protons and secondary electrons for 10% (dotted lines) and 100% (solid lines) of the maximum photo-destruction rate at 1 PAL (top figure, a) and at 2 PAL (bottom figure, b).

References

1. Barrett, G. C., Elmore, D. T. *Amino acids and peptides*. Cambridge; New York: Cambridge University Press (1998).
2. Ringwood, A. E. Chemical Composition of the terrestrial planets. *Geochimica et Cosmochimica Acta* **30**, 41-104 (1996).
3. Summers, D. P., Basa, R. C. B., Khare, B., Rodoni, D. Abiotic Nitrogen Fixation on Terrestrial Planets: Reduction of NO to Ammonia by FeS. *Astrobiology* **12**, 107-114 (2012).
4. Kasting J.F. Bolide impacts and the oxidation state of carbon in the earth's early atmosphere. *Origins Life Evol*. *Biosphere* **20**, 199-231 (1990).
5. Maehara, H., Shibayama, T., Notsu, S., Notsu, Y., Nagao, T., Kusaba, S., Honda, S., Nogami, D., Shibata, K. Superflares on solar-type stars. *Nature* **485**, 478-481 (2012).
6. Shibayama, T., Maehara, H., Notsu, S., Notsu, Y., Nagao, T., Honda, S., Ishii, T. T., Nogami, D., Shibata, K. Superflares on Solar-type Stars Observed with Kepler. I. Statistical Properties of Superflares. *Astrophysical Journal Suppl Ser* **209**, 1-13 (2013).
7. Gopalswamy, N., Xie, H., Yashiro, S., Akiyama, S., Mäkelä, P., Usoskin, I. G. Properties of Ground Level Enhancement Events and the Associated Solar Eruptions During Solar Cycle 23. *Space Sci*. *Rev*. **171**, 23-60 (2012).
8. Tsurutani, B. T., Smith, E. J., Pyle, K. R., Simpson, J. A. Energetic protons accelerated at corotating shocks - Pioneer 10 and 11 observations from 1 to 6 AU. *JGR* **87**, 7389-7404 (1982).

9. Emslie, A. G., Dennis, B. R., Shih, A. Y., Chamberlin, P. C., Mewaldt, R. A.; Moore, C. S., Share, G. H., Vourlidas, A., Welsch, B. T. Global Energetics of Thirty-eight Large Solar Eruptive Events. *Astrophysical Journal* **759**, 1-19 (2012).
10. Miyake, F., Nagaya, K., Masuda, K. & Nakamura, T. A signature of cosmic-ray increase in AD 774-775 from tree rings in Japan. *Nature* **486**, 240-242 (2012).
11. Miyake, F., Masuda, K, Nakamura, T. Another rapid event in the carbon-14 content of tree rings. *Nature Communications* **4:1748**, 1-5 (2013).
12. Tsurutani, B. T., Gonzales, W. D., Lakhina, G. S., Alex, S. The extreme magnetic storm of 1-2 September 1859. *J. Geophys. Res.* **108**, A7, 1268-, (2003).
13. Vidotto, A. A., Gregory, S. G., Jardine, M., Donati, J. F., Petit, P., Morin, J., Folsom, C. P., Bouvier, J., Cameron, A. C., Hussain, G. and 5 co-authors Stellar magnetism: empirical trends with age and rotation. *MNRAS* **441**, 2361-2374 (2014).
14. Airapetian, V., Glocer, A. and Danchi, W. Magnetic Interaction of a Super-CME with the Earth's Magnetosphere: Scenario for Young Earth. *In the 18th Cambridge Workshop on Cool Stars, Stellar Systems, and the Sun Proceeding of Lowell Observatory (9-13 June 2014) Eds. G. van Belle* & H. Harris, 257-268, (2015)
15. Airapetian, V. and Usmanov, A. Reconstructing the Solar Wind from Its Early History to Current Epoch. *Astrophysical Journal* **817**, L24-L30.
16. Tarduno, J., Blackman, E. G. and Mamajek,E. E. Detecting the oldest geodynamo and attendant shielding from the solar wind: Implications for habitability. *Physics of the Earth and Planetary Interiors* **233**, 68-87 (2014).
17. Liu, Y. D., Luhmann, J. G., Kajdič, P., Kilpua, E. K. J., Lugaz, N., Nitta, N. V., Möstl, C., Lavraud, B., Bale, S. D., Farrugia, C. J. & Galvin, A. B. Observations of an extreme

storm in interplanetary space caused by successive coronal mass ejections. *Nature Communications* **5**, pp-pp (2014).

18. Gronoff, G., R., A., Simon W., *C*., Mertens, C. J., Cravens, T. E., & Kallio, E. The precipitation of keV energetic oxygen ions at Mars and their effects during the comet Siding Spring approach. *Geoph*. *Res*. *Lett*. **41**, 4844-4850 (2014).
19. Cnossen, I., Sanz-Forcada, J., Favata, F., Witasse, O., Zegers, T., Arnold, N. F. Habitat of early life: Solar X-ray and UV radiation at Earth's surface 4-3.5 billion years ago. *J*. *Geophys*. *Res*., **112**, E02008 (2007).
20. Claire, M. W., Sheets, J. Cohen, M., Ribas, I., Meadows, V. S., Catling, D. C. The Evolution of Solar Flux from 0.1 nm to 160 μm: Quantitative Estimates for Planetary Studies. *Astrophysical Journal* **57**, 1-12 (2012)
21. Mewaldt, R. A., Looper, M. D., Cohen, C. M. S., Haggerty, D. K., Labrador, A. W., Leske, R. A., Mason, G. M., Mazur, J. E. and von Rosenvinge, T. T. Energy Spectra, Composition, and Other Properties of Ground-Level Events During Solar Cycle 23. *Space Science Reviews* **171**, 97-120 (2012)
22. Goldblatt, C.,Claire, M. W.,Lenton, T. M., Matthews, A. J.,Watson, A, J.Zahnle, Kevin J. Nitrogen-enhanced greenhouse warming on early Earth. *Nature Geoscience* **2**, 891-896 (2009).
23. Nna-Mvondo, D., Navarro-González, R., Raulin, F., Coll, P. Nitrogen Fixation By Corona Discharge On The Early Precambrian Earth. 2005, *Origins Life Evol*. *Biosphere* **35**, 401-409 (2005).
24. Brandvold, D, K., Martinez, P., Hipsh, R. Field measurements of O3 and N2O produced from a corona discharge. *Atmospheric Environment* **30**, 973-976 (1996).

25. Gough, D. O. Solar interior structure and luminosity variations. *Solar Physics* **74**, 21-34 (1981).
26. Kasting, J. F. Early Earth: Faint young Sun redux. *Nature* **464**, 687-689 (2010).
27. Wordsworth, R. and Pierrehumbert, R. Hydrogen-Nitrogen Greenhouse Warming in Earth's Early Atmosphere. *Science*, **339**, 64-67 (2013).
28. Rosing M. T., Bird D. K., Sleep N. H., and Bjerrum C. J. No climate paradox under the faint early Sun. *Nature* **464**, 744-747 (2010).
29. Miyakawa, S., Cleaves, Cleaves, H. J., and Miller, S. L. The Cold Origin of Life: B. Implications Based on Pyrimidines and Purines Produced From Frozen Ammonium Cyanide Solutions. *Orig Life Evol Biosph* **32**, 209-218 (2002).

ACKNOWLEDGEMENTS: We thank three referees for constructive suggestions that improved the manuscript. This work was supported by NASA GSFC Science Task Group funds. V. Airapetian performed the part of this work while staying at ELSI/Tokyo Tech.

CORRESPONDING AUTHOR:
Correspondence and requests for materials regarding this paper should be addressed to Dr. Vladimir Airapetian, NASAGSFC, Code 671, 8800 Greenbelt Rd, Greenbelt, MD 20771, E-mail: Vladimir.Airapetian@nasa.gov.

AUTHOR CONTRIBUTIONS:
V. Airapetian conceived and designed the numerical models, analyzed the data, contributed materials and wrote the manuscript. A. Glocer and G. Gronoff contributed to the

development and execution of codes and data analysis. E. Hébrard contributed to the chemistry model and data analysis, W. Danchi contributed to data analysis and proofreading of the paper.

Competing financial interests.

The authors declare no competing financial interests.

FIGURE CAPTIONS.

Figure 1. The initial (left panel, a) and the final state (right panel, b) magnetic field lines in white) and the plasma pressure (in color) of the Earth's magnetosphere due to the CME event [14].

Figure 2. XUV flux of the young Sun at 0.7 Gyr [20].

Figure 3. The pathway diagram of abiotic production of odd nitrogen and nitrogen-bearing compounds including nitrous oxide and hydrogen cyanide due to photo and collisional dissociation and ionizations caused by XUV solar flux and SEP particle flux.

Figure 4. Radial profiles of the steady-state mixing ratios of various species produced by incoming flux of primary protons and secondary electrons for 10% (dotted lines) and 100% (solid lines) of the maximum photo-destruction rate at 1 PAL (top figure, 4a) and at 2 PAL (bottom figure, 4b).

METHODS

1. SWMF DESCRIPTION

In this paper, we utilized the Space Weather Modeling Framework (SWMF) available at Community Coordinated Modeling Center (CCMC) at NASA Goddard Space Flight Center (see at http://ccmc.gsfc.nasa.gov). A single-fluid, time dependent fully non-linear 3D magnetohydrodynamic (MHD) code BATS-R-US (Block-Adaptive-Tree Solar-wind Roe-type Upwind Scheme) is a part of SWMF and was developed at the University of Michigan Center of Space Environment Modeling (CSEM). The spine of the SWMF is the BATS-R-US code [30,31], which is coupled to Rice Convection Model (RCM, [31] to model a propagation and interaction of a model SCME with a magnetosphere and ionosphere of a young Earth. The MHD part of the code calculates the dynamic response of the large-scale magnetospheric plasma to varying solar wind conditions in a self consistent manner by using the block-adaptive wind Roe-type upwind scheme global MHD code [30]. The dynamics of the magnetosphere is described in a Cartesian geometry by using resistive MHD equations. The electromagnetic coupling of the magnetosphere to a conducting ionosphere is handled in a standard way [32]. Specifically, the magnetospheric currents near the inner boundary of the MHD simulation are mapped to the ionosphere where. A potential solver is then used which combines these currents with a conductance map of the ionosphere (including solar and auroral contributions) to produce the electric potential in the ionosphere. That potential is then used to set the electric field and corresponding drift at the magnetospheric simulations inner boundary.

The MHD approximation does not provide an adequate description of the inner magnetosphere because energy dependent particle drifts and ring current evolution become

important. Here we use the Rice Convection Model, embedded in the MHD simulation, to model this important region [31]. The RCM code is a kinetic plasma model that couples plasma motions in the inner magnetosphere and calculates the energy dependent particle drifts and ring current evolution in the inner magnetosphere. The ring current carries the most of the energy density during magnetic storms and is essential to modeling strong storms. This coupling is crucial for description of solar wind effects on a magnetosphere, because the ionosphere provides closure of magnetospheric currents, which is needed for realistic description of magnetospheric convection and associated electric fields. Thus, we apply a dedicated inner magnetospheric model that is fully coupled to the MHD code for the treatment of the inner magnetosphere. We simulate the magnetospheric cavity (outer and inner magnetosphere) in a computational box defined by the following dimensions $-224R_E < x < 224R_E$, $-128R_E < y < 128R_E$, $-128R_E < z < 128R_E$, where R_E is the radius of the Earth placed at the center of the computational box. The dipole tilt is neglected in this problem. The simulations were carried out using a block adaptive high-resolution grid with the minimum cell size of 1/16 R_E.

The inner boundary is set at 1.25 R_E with a density of 100 cm^{-3}. The velocity at the inner body is set to the $\vec{E} \times \vec{B}$ velocity, where $\vec{E}$ is determined from the ionospheric potential and B is the Earth's magnetic field. The pressure is set to float. The magnetic field is set in a way that the radial component is the Earth's dipole and the tangential components are allowed to float. The simulation is initialized with a dipole everywhere in the computational domain and a small density, zero velocity, and a finite pressure. The solar wind conditions are set at the upstream boundary and some period of local time stepping is used to get an initial steady state solution. We assume the solar wind input parameters including the three components of

346 interplanetary magnetic field, B_X, B_Y and B_Z, the plasma density and the wind velocity, V_X,
347 using the physical conditions associated with a Carrington- type event as discussed by [33] and
348 [14], see Figure 1. The time evolution of the plasma pressure (in nPa) and current density (in
349 microAmps/m^2) during the extreme CME event are presented in the attached Movie 1.

350 ## 2. AEROPLANETS MODEL DESCRIPTION

351 We used our sophisticated Aeroplanets model with enhanced chemistry [18] to model the upper
352 atmospheric region (up to 200 km) in response to young Sun's XUV (X-ray and EUV) emission
353 from and precipitating electrons and protons due to an SEP event. The model calculates the
354 photo and collisional (due to protons) dissociation, ionization and photoexcitation processes in
355 the Earth's atmosphere. The primary photoelectrons are then transported along a magnetic field
356 line, and the electron impact is computed solving the stationary kinetic Boltzmann equation. This
357 results in the dissociation, ionization and excitation of the different atmospheric species. The
358 Aeroplanets code incorporates 117 chemical reactions with the rates presented in Table 1.
359 To converge to steady state chemical solution for the early Earth atmosphere described in the
360 Main section was reached after running the code for 6 months of physical time.
361

362 **Table 1. List of Chemical Reactions Used in Our Model**

Reaction	**Reaction rate (in cgs units)**
H + CH -> C + H2	0.124E-09 * (T / 300) ** (0.260E+00)
H + CH2 -> CH + H2	0.220E-09 * (T / 300) ** (0.320E+00)

H + e3CH2 -> CH + H2	0.220E-09 * (T / 300) ** (0.320E+00)
H + CH3 -> e3CH2 + H2	0.100E-09 * exp(-0.760E+04 / T)
H + CH4 -> CH3 + H2	0.589E-12 * (T / 300) ** (0.300E+01) * exp(-0.404E+04 / T)
CH + H2 -> e3CH2 + H	0.310E-09 * exp(-0.165E+04 / T)
CH + CH -> C2H + H	2.00E-10
CH + CH -> e3CH2 + C	2.00E-11
CH + e3CH2 -> C2H2 + H	2.00E-10
CH + CH3 -> C2H3 + H	1.00E-11
CH + CH3 -> C2H2 + H + H	1.00E-10
CH + CH4 -> C2H4 + H	0.105E-09 * (T / 300) ** (-0.104E+01) * exp(-0.361E+02 / T)
CH2 + H2 -> CH3 + H	0.880E-10 * (T / 300) ** (0.350E+00)
CH2 + CH4 -> e3CH2 + CH4	0.310E-11 * exp(0.250E+03 / T)
CH2 + CH4 -> CH3 + CH3	0.279E-10 * exp(0.250E+03 / T)
CH2 + C2H2 -> e3CH2 + C2H2	2.30E-10
CH2 + C2H2 -> C3H3 + H	0.760E-10 * (T / 300) ** (-0.300E+00)

CH2 + N2 -> e3CH2 + N2	0.110E-10 * (T / 300) ** (0.810E+00)
e3CH2 + H2 -> CH3 + H	0.800E-11 * exp(-0.450E+04 / T)
e3CH2 + CH4 -> CH3 + CH3	0.713E-11 * exp(-0.505E+04 / T)
CH3 + H2 -> CH4 + H	0.245E-13 * (T / 300) ** (0.288E+01) * exp(-0.460E+04 / T)
N(4S) + CH -> CN + H	0.140E-09 * (T / 300) ** (0.410E+00)
N(4S) + e3CH2 -> HCN + H	0.500E-10 * (T / 300) ** (0.170E+00)
N(4S) + e3CH2 -> HNC + H	0.300E-10 * (T / 300) ** (0.170E+00)
N(4S) + CH3 -> H2CN + H	5.60E-11
N(4S) + CH3 -> HCN + H + H	6.00E-12
N(4S) + NH -> N2 + H	0.250E-10 * (T / 300) ** (0.170E+00)
N(4S) + CN -> C + N2	0.900E-10 * (T / 300) ** (0.420E+00)
N(4S) + H2CN -> N2 + e3CH2	4.00E-11
N(4S) + H2CN -> HCN + NH	5.00E-12
N(2D) -> N(4S)	2.30E-05
N(2D) + H2 -> NH + H	0.420E-10 * exp(-0.880E+03 / T)
N(2D) + CH4 -> NH + CH3	0.130E-10 * exp(-0.755E+03 / T)

N(2D) + CH4 -> CH2NH + H	0.350E-10 * exp(-0.755E+03 / T)
N(2D) + N2 -> N(4S) + N2	0.100E-12 * exp(-0.520E+03 / T)
N(2D) + NH3 -> N2H2 + H	5.00E-11
N(2D) + HCN -> CH + N2	5.00E-11
N(2D) + HNC -> CN2 + H	2.00E-11
N(2D) + HNC -> CH + N2	2.00E-11
NH + H -> N(4S) + H2	0.220E-11 * (T / 300) ** (0.155E+01) * exp(-0.103E+03 / T)
NH + CH -> HCN + H	5.00E-11
NH + CH -> HNC + H	5.00E-11
NH + e3CH2 -> H2CN + H	3.00E-11
NH + e3CH2 -> HCN + H + H	3.00E-11
NH + e3CH2 -> HNC + H2	5.00E-12
NH + CH3 -> CH2NH + H	0.130E-09 * (T / 300) ** (0.170E+00)
NH + NH -> N2 + H + H	2.00E-10
NH + NH2 -> N2H2 + H	0.100E-09 * (T / 300) ** (0.170E+00)
NH + CN -> CN2 + H	1.00E-10

NH + CN -> N2 + CH	1.00E-10
NH2 + H2 -> NH3 + H	0.209E-11 * exp(-0.428E+04 / T)
NH2 + H -> NH + H2	0.200E-10 * exp(-0.240E+04 / T)
NH2 + CH4 -> NH3 + CH3	0.399E-13 * (T / 300) ** (0.359E+01) * exp(-0.454E+04 / T)
NH2 + C2H2 -> NH3 + C2H	0.111E-12 * exp(-0.185E+04 / T)
NH2 + C2H3 -> NH3 + C2H2	2.00E-11
NH2 + C2H3 -> SOOTN + H	8.00E-11
NH2 + H2CN -> HCN + NH3	0.540E-10 * (T / 300) ** (-0.110E+01) * exp(-0.600E+02 / T)
NH3 + H -> NH2 + H2	0.423E-13 * (T / 300) ** (0.393E+01) * exp(-0.406E+04 / T)
NH3 + CH -> CH2NH + H	0.169E-09 * (T / 300) ** (-0.560E+00) * exp(-0.280E+02 / T)
NH3 + CH3 -> NH2 + CH4	0.510E-13 * (T / 300) ** (0.286E+01) * exp(-0.734E+04 / T)
CN + H2 -> HCN + H	0.412E-12 * (T / 300) ** (0.287E+01) * exp(-0.820E+03 / T)
CN + CH -> HCN + C	0.100E-09 * (T / 300) ** (-0.170E+00)
CN + e3CH2 -> HCN + CH	5.00E-11

CN + e3CH2 -> CHCN + H	5.00E-11
CN + e3CH2 -> C2N + H2	5.00E-11
CN + CH3 -> CH2CN + H	1.00E-10
CN + CH4 -> HCN + CH3	0.620E-11 * exp(-0.721E+03 / T)
CN + NH3 -> HCN + NH2	0.277E-10 * (T / 300) ** (-0.114E+01)
CN + HCN -> C2N2 + H	0.430E-12 * (T / 300) ** (0.171E+01) * exp(-0.770E+03 / T)
CN + HNC -> C2N2 + H	2.00E-10
HCN + CH -> CHCN + H	0.140E-09 * (T / 300) ** (-0.170E+00) * exp(-0.0 / T)
HCN + CH -> C2N + H2	0.140E-09 * (T / 300) ** (-0.170E+00) * exp(-0.0 / T)
HCN + 1C2 -> C3N + H	0.200E-09 * (T / 300) ** (0.170E+00) * exp(-0.0 / T)
HNC + H -> HCN + H	0.300E-10 * exp(-0.800E+03 / T)
H2CN + H -> HCN + H2	6.00E-11
H2CN + CH3 -> CH4 + HCN	3.00E-11
O(3P) + CH2 -> HCO + H	1.00E-11
O(3P) + CH2 -> CO + H + H	5.00E-11
O(3P) + CH2 -> CO + H2	6.00E-11

O(3P) + e3CH2 -> HCO + H	1.00E-11
O(3P) + e3CH2 -> CO + H + H	5.00E-11
O(3P) + e3CH2 -> CO + H2	6.00E-11
O(3P) + CH3 -> CO + H2 + H	2.90E-11
O(3P) + CH3 -> H2CO + H	1.10E-10
O(3P) + NH -> NO + H	6.60E-11
O(3P) + HNO -> OH + NO	3.80E-11
O(1D) + H2 -> OH + H	1.10E-10
O(1D) + CH4 -> OH + CH3	1.05E-10
O(1D) + CH4 -> CH3O + H	3.50E-11
O(1D) + CH4 -> H2CO + H2	7.50E-12
O(1D) + N2 -> O(3P) + N2	2.15E-11
OH + H2 -> H2O + H	0.280E-11 * exp(-0.180E+04 / T)
OH + CH4 -> H2O + CH3	0.185E-11 * exp(-0.169E+04 / T)
OH + N(4S) -> NO + H	4.50E-11
OH + N(2D) -> NO + H	4.50E-11

OH + CO -> CO2 + H	1.30E-13
H2O + CH -> H2CO + H	0.280E-10 * (T / 300) ** (-0.122E+01) * exp(-0.120E+02 / T)
H2O + N(2D) -> OH + NH	4.50E-11
H2O + N(2D) -> HNO + H	5.00E-12
CO2 + N(2D) -> CO + NO	0.100E-10 * exp(-0.100E+04 / T)
NO + CH -> HCN + O(3P)	0.100E-09 * (T / 300) ** (-0.130E+00)
NO + CH -> NCO + H	0.300E-10 * (T / 300) ** (-0.130E+00)
NO + CH -> CO + NH	0.300E-10 * (T / 300) ** (-0.130E+00)
NO + CH -> OH + CN	0.100E-10 * (T / 300) ** (-0.130E+00)
NO + e3CH2 -> HNCO + H	0.210E-11 * exp(0.554E+03 / T)
NO + e3CH2 -> CO + NH2	0.300E-12 * exp(0.554E+03 / T)
NO + N(4S) -> O(3P) + N2	0.400E-10 * (T / 300)
NO + N(2D) -> O(3P) + N2	0.600E-10 * (T / 300)
NO + NH -> N2O + H	0.290E-10 * (T / 300) ** (-0.300E+00) * exp(0.770E+02 / T)
NO + NH -> OH + N2	0.120E-10 * (T / 300) ** (-0.300E+00) * exp(0.770E+02 / T)

HNO + H -> NO + H2	0.310E-10 * exp(-0.500E+03 / T)
HNO + N(2D) -> NO + NH	5.00E-11
N2O + CH -> NO + HCN	0.150E-10 * exp(0.257E+03 / T)
N2O + N(2D) -> N2 + NO	0.150E-10 * exp(-0.570E+03 / T)
H + H -> H2	(0.914E-32 * (T / 300) ** (-0.600E+00) * exp(-0.0 / T))* [M] / (1 + (0.914E-32 * (T / 300) ** (-0.600E+00) * exp(-0.0 / T))* [M] / (0.100E-09 * exp(-0.0 / T)))
H + CH3 -> CH4	(0.890E-28 * (T / 300) ** (-0.180E+01) * exp(-31.8 / T))* [M] / (1 + (0.890E-28 * (T / 300) ** (-0.180E+01) * exp(-31.8 / T))* [M] / (0.320E-09 * (T / 300) ** (0.133E+00) * exp(-2.54 / T)))
HCN + H -> H2CN	(0.100E-33 * exp(-0.0 / T))* [M] / (1 + (0.100E-33 * exp(-0.0 / T))* [M] / (0.980E-11 * exp(-2080.0 / T)))

References

30. Powell, K. G., Roe, P. L., Linde, T. J., Gombosi, T. I., De Zeeuw, D. L. A Solution-Adaptive Upwind Scheme for Ideal Magnetohydrodynamics. *J*. *Comp*. *Phys*. **154**, 284-309 (1999).

31. de Zeeuw, D. L., Sazykin, S., Wolf, R. A., Gombosi, T. I., Ridley, A. J., Toth, G. Coupling of a global MHD code and an inner magnetospheric model: Initial results. *J*.

Geophys. *Res*. **109**, A12219 (2004).

32. Ridley, A. J., Hansen, K. C., Toth, G., de Zeeuw, D. L., Gombosi, T. I., Powell, K. G. University of Michigan MHD results of the Geospace Global Circulation Model metrics challenge. *J*. *Geophys*. *Res*., 107, 1290- (2002).

33. Ngwira, C. M., Pulkkinen, A., Kuznetsova, M. M., Glocer, A. Modeling extreme "Carrington-type" space weather events using three-dimensional global MHD simulations *J*. *Geophys*. *Res*.*: Space Physics* **119**, 4456-4474 (2014).

Code availability. BATS-R-US code as a part of SWMF used to generate the scenario shown in Figure 1 can be accessed through GSFC's CCMC run-on-request web site at http://ccmc.gsfc.nasa.gov. We have opted not to make the computer code, Aeroplanets, associated with this paper available because we are currently in the phase of adopting it for free access at Exoplanetary part of CCMC's web site. The authors declare that model data supporting the findings of this study are available within the article and its supplementary information. Other model related data will be available on request from the authors.